JOURNAL OF AIRCRAFT
Vol. 38, No. 2, March–April 2001

Navier–Stokes Computations of Limit-Cycle Oscillations for a B-1-Like Configuration

Peter M. Hartwich,* Steven K. Dobbs,† Alan E. Arslan,‡ and Suk C. Kim§
The Boeing Company, Long Beach, California 90807-4418

A nonlinear aeroelastic analysis method that solves for the Navier–Stokes equations is put to test in an attempt to capture a limit-cycle oscillation (LCO) phenomenon that is characterized by a coupling of aerodynamic forces due to vortical flow with the elastic response of a wing structure. Time-accurate solutions are computed for unsteady, transonic ($M_\infty = 0.975$), and viscous ($Re_c = 5.9 \times 10^6$) flows over a B-1-like wing-body configuration at angles of attack of 7.38, 7.88, 8.00, 8.13, 8.25, and 8.38 deg. All flowfield solutions are obtained with the CFL3D Euler/Navier–Stokes solver that was extensively modified for strongly coupled nonlinear aeroelastic analyses. Phase diagrams and aerodynamic damping estimates are used to identify LCO. The predicted aerodynamic damping appears to capture the trends of the experimental data. There is a good correlation between experimental oilflow images and computed instantaneous streamline patterns. The computed amplitude of the wing structural response is much smaller than indicated by flight and wind-tunnel tests. The choice of the computational time step size is identified as a major factor in modeling the development of LCO.

Introduction

THE modeling of the interaction between aerodynamic and structural phenomena has become commonplace for flight regimes where aerodynamics and structures can both be modeled as linear systems. As long as this basic assumption applies, static and dynamic aeroelastic effects can be accurately and inexpensively predicted using software packages that combine a linear finite element formulation[1] for modeling the structural dynamics with linear aerodynamics theory such as a doublet-lattice method.[2] This approach fails as structures and/or aerodynamics become nonlinear. Examples of such instances are transonic flutter, control surface buzz, and limit-cycle oscillations (LCO).

Over the years, several attempts have been made to produce a nonlinear aeroelastic analysis capability by coupling advanced Euler/Navier–Stokes solvers with computational structures methods. Recently, an academia/government/industry consortium, called Aerodynamics–Structures–Control Interaction, has set out to evaluate several of these nonlinear aeroelastic analysis methods in the following five categories: 1) static aeroelasticity, 2) transonic flutter, 3) LCO with shocks, 4) LCO with separation/vortices, and 5) buzz. As part of this evaluation effort, this paper highlights some experiences with applications of an aeroelastic version of the Euler/Navier–Stokes CFL3D[3–5] code to simulations of the B-1 LCO phenomenon.

This LCO problem was chosen as a test case because there is an extensive experimental database available[6] and because it still awaits a successful simulation using nonlinear aeroelastic analysis. Several years ago, Guruswamy[7] used his state-of-the-art ENSAERO method to tackle this computational challenge. For static aeroelastic cases, Guruswamy's computed flowfield results correlated well with experimental data, yet his dynamic aeroelastic analysis fell short of capturing the LCO phenomenon. Two conjectures were offered to explain this shortfall: insufficient geometric fidelity in gridding the outer wing portion and the lack of suitable turbulence models to model unsteady vortical flow. The present study made an effort to model the outer wing section accurately, that is, the swing wing. There is still no way of addressing the second conjecture. The experience has been that the algebraic Baldwin–Lomax model with the so-called Degani–Schiff modifications still is the standard for modeling steady vortical flows. It might be insufficient for modeling unsteady vortical flow, yet its more modern and computationally more expensive competitors show at best similar, yet mostly poorer, performance in modeling steady vortical flow. That makes for no good case to expect superior performance for accurately computing unsteady vortical flow.

Along with the various releases of the CFL3D code, several aeroelastic versions of CFL3D have been developed.[8–11] The aeroelastic version of the CFL3D method used in this study has been developed under the NASA/Industry High-Speed Research (HSR) program, where it was heavily used for generating nonlinear loads, simulating flutter,[12] and assessing static aeroelastic effects on aerodynamic performance.[13] In the HSR program, the CFL3D method was selected for further improvement of its aeroelastic modeling capabilities because it offered, at the time this decision was made, the most versatility. Compared to other public-domain Euler/Navier–Stokes methods, the CFL3D solver offered more turbulence models; it could handle blocked, overlapped, and embedded multizone structured grids; and it came with an advanced time-integration algorithm for computing solutions to unsteady flow.[14]

Next, brief discussions are offered of some salient technical features of the aeroelastic version of CFL3D employed in the present studies. These discussions are intended to set expectations about the capabilities and the limitations of this method. Thereafter, results will be presented for time-accurate solutions for unsteady, transonic ($M_\infty = 0.975$), and viscous ($Re_c = 5.9 \times 10^6$, where c is the mean aerodynamic chord) flows over a B-1-like wing/body configuration at angles of attack of 7.38, 7.88, 8.00, 8.13, 8.25, and 8.38 deg. The process for obtaining dynamic aeroelastic solutions will be described. Phase diagrams and aerodynamic damping estimates are used to identify LCO, and some light will be shed on the selection of proper computational time step sizes for modeling the development of LCO.

Received 25 April 2000; presented as Paper 2000-2338 at the AIAA FLUIDS Conference, Denver, CO, 19–22 June 2000; revision received 28 August 2000; accepted for publication 5 September 2000.

*Associate Technical Fellow, High Speed Aerodynamics Technology, Phantom Works, Mail Code C078-0532, 2401 E. Wardlow Road. Associate Fellow AIAA.

†Program Manager, Global Integrated Lines, Loads, and Laws, Phantom Works, Mail Code C078-0209, 2401 E. Wardlow Road. Senior Member AIAA.

‡Engineer/Scientist Specialist, Stability and Control, Phantom Works, Mail Code C078-0420, 2401 E. Wardlow Road. Senior Member AIAA.

§Senior Engineer/Scientist, High Speed Aerodynamics Technology, Phantom Works, Mail Code C078-0532, 2401 E. Wardlow Road.

Technical Approach

Solution Process

This study was conducted with a closely coupled nonlinear aeroelastic analysis methodology. The coupling of a computational structures method (CSM) with a computational fluid dynamics (CFD) method was based on the approach in the CAP-TSD code.[15] Recalling that the CAP-TSD method uses a predictor–corrector CSM, the time integration at each time level $(n+1)$ involves 1) predicting (estimating) structural displacements using flow and structures information from time levels (n) and $(n-1)$, 2) adjusting computational surface and volume grids, 3) updating metric terms and Jacobians, 4) updating flow boundary conditions (body surface speeds, Navier–Stokes solutions only), 5) computing the solution to Euler/Navier–Stokes equations at time level $(n+1)$, 6) recomputing structural loads with solution from step 5, and 7) correcting structural displacements.

Equations of Structural Motion

As proposed by Cunningham et al.,[15] the equations of structural motion are derived by assuming that they can be described by a separation of time and space variables in a truncated finite modal series. This modal series consists of a summation of the free vibration modes $\boldsymbol{h}_i$ weighted by the generalized displacement $\boldsymbol{q}_i$ such that

$$\delta_x(\boldsymbol{x},\boldsymbol{y},\boldsymbol{z},\boldsymbol{t}) = \sum_{i=1}^{n} \boldsymbol{q}_i(\boldsymbol{t})\boldsymbol{h}_{x_i}(\boldsymbol{x},\boldsymbol{y},\boldsymbol{z})$$

$$\delta_y(\boldsymbol{x},\boldsymbol{y},\boldsymbol{z},\boldsymbol{t}) = \sum_{i=1}^{n} \boldsymbol{q}_i(\boldsymbol{t})\boldsymbol{h}_{y_i}(\boldsymbol{x},\boldsymbol{y},\boldsymbol{z})$$

$$\delta_z(\boldsymbol{x},\boldsymbol{y},\boldsymbol{z},\boldsymbol{t}) = \sum_{i=1}^{n} \boldsymbol{q}_i(\boldsymbol{t})\boldsymbol{h}_{z_i}(\boldsymbol{x},\boldsymbol{y},\boldsymbol{z}) \tag{1}$$

where δ_x, δ_y, and δ_z are the structural deflections and $\boldsymbol{h}_x$, $\boldsymbol{h}_y$, and $\boldsymbol{h}_z$ are the modal deflections for mode i in each coordinate direction. After applying Lagrange's equation to this system, the structural equations of motion for each mode i assume

$$\boldsymbol{m}_i\ddot{\boldsymbol{q}}_i + \boldsymbol{g}_i\dot{\boldsymbol{q}}_i + \boldsymbol{k}_i\boldsymbol{q}_i = \boldsymbol{Q}_i \tag{2}$$

where $\boldsymbol{m}_i$ is the generalized mass, $\boldsymbol{g}_i$ is the generalized damping, $\boldsymbol{k}_i$ is the generalized stiffness, and $\boldsymbol{Q}_i$ is the generalized aerodynamic force computed by integrating the local surface pressure coefficients weighted by the mode shapes. The generalized aerodynamic force $\boldsymbol{Q}_i$ for each mode i is given by

$$\boldsymbol{Q}_i = -\frac{1}{2}\rho_\infty \boldsymbol{V}_\infty^2 \int_S \boldsymbol{C}_p(\boldsymbol{n}_x\boldsymbol{h}_{x_i} + \boldsymbol{n}_y\boldsymbol{h}_{y_i} + \boldsymbol{n}_z\boldsymbol{h}_{z_i})\,\mathrm{d}\boldsymbol{S} \tag{3}$$

The solution to each normal mode equation in Eq. (2) is sketched in Ref. 15. For the sake of completeness, a detailed description of the time-marching solution process is provided here. Recasting Eq. (2) as

$$\ddot{\boldsymbol{q}}_i + \boldsymbol{m}_i^{-1}\boldsymbol{g}_i\dot{\boldsymbol{q}}_i + \boldsymbol{m}_i^{-1}\boldsymbol{k}_i\boldsymbol{q}_i = \boldsymbol{m}_i^{-1}\boldsymbol{Q}_i \tag{4}$$

permits formulating the equations of structural motion in first-order state-space form:

$$\dot{\boldsymbol{x}}_i = \boldsymbol{A}\boldsymbol{x}_i + \boldsymbol{B}\boldsymbol{Q}_i \tag{5}$$

where

$$\boldsymbol{x}_i = \begin{pmatrix}\boldsymbol{q}_i\\ \dot{\boldsymbol{q}}_i\end{pmatrix}, \qquad \boldsymbol{A} = \begin{pmatrix}\boldsymbol{0} & 1\\ -\boldsymbol{m}_i^{-1}\boldsymbol{k}_i & -\boldsymbol{m}_i^{-1}\boldsymbol{g}_i\end{pmatrix}, \qquad \boldsymbol{B} = \begin{pmatrix}0\\ -\boldsymbol{m}_i^{-1}\end{pmatrix} \tag{6}$$

Equation (6) is a finite-dimensional linear differential equation whose solution is given by

$$\boldsymbol{x}_i(\boldsymbol{t}) = \Phi(\boldsymbol{t})\boldsymbol{x}_i(\boldsymbol{t}=\boldsymbol{0}) + \int_0^t e^{A(t-\tau)}\boldsymbol{B}\boldsymbol{Q}_i(\tau)\,\mathrm{d}\tau \tag{7}$$

In general, the state-transition matrix Φ can be calculated to any level of accuracy by including a sufficient number of terms of a series expansion of this matrix exponential function. Because the aeroelastic problem here assumes normal modes, a closed-form expression for each element of the state-transition matrix Φ is available,[15]

$$\varphi_{11} = e^{at}\cos(\boldsymbol{bt}) - (\boldsymbol{a}/\boldsymbol{b})e^{at}\sin(\boldsymbol{bt})$$

$$\varphi_{21} = -[(\boldsymbol{a}^2+\boldsymbol{b}^2)/\boldsymbol{b}]e^{at}\sin(\boldsymbol{bt}), \qquad \varphi_{12} = (1/\boldsymbol{b})e^{at}\sin(\boldsymbol{bt})$$

$$\varphi_{22} = e^{at}\cos(\boldsymbol{bt}) + (\boldsymbol{a}/\boldsymbol{b})e^{at}\sin(\boldsymbol{bt}) \tag{8}$$

with

$$\boldsymbol{a} = -\boldsymbol{g}_i/2, \qquad \boldsymbol{b} = \left[\boldsymbol{k}_i/\boldsymbol{m}_i + \boldsymbol{a}^2\right]^{0.5}$$

As proposed in Ref. 15, Eq. (7) is integrated between any two subsequent time levels, $\boldsymbol{n}$ and $\boldsymbol{n}+1$, by

$$\boldsymbol{x}_i[(\boldsymbol{n}+1)\Delta\boldsymbol{t}] = \Phi(\Delta\boldsymbol{t})\boldsymbol{x}_i(\boldsymbol{n}\Delta\boldsymbol{t}) + \int_{n\Delta t}^{(n+1)\Delta t} \exp\{A[(\boldsymbol{n}+1)\Delta\boldsymbol{t}-\tau]\}\boldsymbol{B}\boldsymbol{Q}_i(\tau)\,\mathrm{d}\tau \tag{9}$$

If $\boldsymbol{Q}_i$ varies linearly in any time interval $\Delta\boldsymbol{t}$, Eq. (9) is solved using a predictor–corrector scheme that first extrapolates $\boldsymbol{Q}_i$ to predict a preliminary displacement

$$\tilde{\boldsymbol{x}}_i^{n+1} = \Phi\boldsymbol{x}_i^n + \Theta\left(3\boldsymbol{Q}_i^n - \boldsymbol{Q}_i^{n-1}\right)/2 \tag{10}$$

The results from Eq. (10) are used to update the flowfield solution and to evaluate the loads $\tilde{\boldsymbol{Q}}_i^{n+1}$. These values are then used in the corrector step to compute

$$\boldsymbol{x}_i^{n+1} = \Phi\boldsymbol{x}_i^n + \Theta\left(\tilde{\boldsymbol{Q}}_i^{n+1} + \boldsymbol{Q}_i^n\right)/2 \tag{11}$$

The elements of the integrated state-transition matrix Θ are

$$\Theta_{11} = [e^{a\Delta t}/(\boldsymbol{a}^2+\boldsymbol{b}^2)][2\boldsymbol{a}\cos(\boldsymbol{b}\Delta\boldsymbol{t}) + (\boldsymbol{b}-\boldsymbol{a}^2/\boldsymbol{b})\sin(\boldsymbol{b}\Delta\boldsymbol{t}) - 2\boldsymbol{a}]$$

$$\Theta_{12} = [e^{a\Delta t}/(\boldsymbol{a}^2+\boldsymbol{b}^2)][(\boldsymbol{a}/\boldsymbol{b})\sin(\boldsymbol{b}\Delta\boldsymbol{t}) - \cos(\boldsymbol{b}\Delta\boldsymbol{t})] - 1/(\boldsymbol{a}^2+\boldsymbol{b}^2)$$

$$\Theta_{21} = (e^{a\Delta t}/\boldsymbol{b})[\boldsymbol{b}\cos(\boldsymbol{b}\Delta\boldsymbol{t}) - \boldsymbol{a}\sin(\boldsymbol{b}\Delta\boldsymbol{t})] - 1$$

$$\Theta_{22} = [e^{a\Delta t}/(\boldsymbol{a}^2+\boldsymbol{b}^2)][(\boldsymbol{b}+\boldsymbol{a}^2/\boldsymbol{b})\sin(\boldsymbol{b}\Delta\boldsymbol{t})] \tag{12}$$

Note that both Φ and Θ depend only on structural properties and on the constant user-specified time step size $\Delta\boldsymbol{t}$. Thus, both Φ and Θ only need to be computed at the beginning of an aeroelastic solution. Also, note that Eq. (10), taken together with the solution process at the beginning of this section, implies $\boldsymbol{Q}_i^n = \tilde{\boldsymbol{Q}}_i^n$. This linearization, although following established standards for aeroelastic versions of CFL3D, reduces the solution of Eq. (9) back to first order, negating the benefits of the predictor–corrector approach. Future implementors of this coupling of structures and aerodynamics might want to improve on this process.

Governing Equations of Flow

The CFL3D method solves for the Euler/Navier–Stokes equations, which are written here as

$$\frac{1}{\boldsymbol{J}}\frac{\partial\boldsymbol{Q}}{\partial\boldsymbol{t}} = R(\boldsymbol{Q}) \tag{13}$$

where $\boldsymbol{J}$ is the Jacobian of the transformation from physical to curvilinear body-conforming coordinates, $\boldsymbol{Q}$ the vector of dependent flow

variables (i.e., mass, momentum, and energy), and R the so-called right-hand side

$$R = -\left[\frac{\partial(\boldsymbol{F}-\boldsymbol{F}_v)}{\partial\xi} + \frac{\partial(\boldsymbol{G}-\boldsymbol{G}_v)}{\partial\eta} + \frac{\partial(\boldsymbol{H}-\boldsymbol{H}_v)}{\partial\zeta}\right] \tag{14}$$

with the inviscid and viscous (subscript v) flux terms. Details of the equations can readily be found in Refs. 3–5 and 14. For reasons of numerical stability, the τ–TS method, which uses subiterations at each time level to remove linearization errors, is employed for the time integration. This method needs to be modified to accommodate the changes in the Jacobians as the dynamic mesh adjusts to the aeroelastic deformations of a subject vehicle configuration:

$$(1/\Delta\tau)(\boldsymbol{Q}^{m+1}/\boldsymbol{J}^{m+1} - \boldsymbol{Q}^{m}/\boldsymbol{J}^{m}) + (1/\Delta t)[(1+\Psi)(\boldsymbol{Q}^{m+1}/\boldsymbol{J}^{m+1} - \boldsymbol{Q}^{n}/\boldsymbol{J}^{n}) - \Psi(\boldsymbol{Q}^{n}/\boldsymbol{J}^{n} - \boldsymbol{Q}^{n-1}/\boldsymbol{J}^{n-1})] = R(\boldsymbol{Q}^{m+1}) \tag{15}$$

where $\Delta\tau$ is the pseudo time step size, Δt is the physical time step size, the superscript n denotes the physical time level, and the solution to Eq. (15) is subiterated in m. When $\Psi = \mathbf{0}$, the method is first-order temporally accurate; when $\Psi = \frac{1}{2}$, the method is second-order accurate. As $m \to \infty$, the pseudo time term vanishes, and $(\boldsymbol{Q}/\boldsymbol{J})^{m+1} \to (\boldsymbol{Q}/\boldsymbol{J})^{n+1}$. On applying the chain rule, some rearranging, and linearizing R as

$$R(\boldsymbol{Q}^{m+1}) \cong R(\boldsymbol{Q}^{m}) + \frac{\partial R}{\partial \boldsymbol{Q}}\Delta\boldsymbol{Q}^{m} \tag{16}$$

Eq. (15) assumes

$$\frac{\Delta^m\boldsymbol{Q}}{\boldsymbol{J}^{n+1}\Delta\tau} + \frac{\boldsymbol{Q}^n}{\Delta\tau}\left(\frac{1}{\boldsymbol{J}^{m+1}} - \frac{1}{\boldsymbol{J}^{m}}\right) + \frac{1+\Psi}{\boldsymbol{J}^{n+1}\Delta t}\Delta^m\boldsymbol{Q} = R(\boldsymbol{Q}^{m+1}) + \frac{\Psi}{\Delta t}\left[\left(\frac{\boldsymbol{Q}}{\boldsymbol{J}}\right)^{n} - \left(\frac{\boldsymbol{Q}}{\boldsymbol{J}}\right)^{n-1}\right] - \frac{(1+\Psi)\boldsymbol{Q}^n}{\Delta t}\left(\frac{1}{\boldsymbol{J}^{n+1}} - \frac{1}{\boldsymbol{J}^{n}}\right) - \frac{1+\Psi}{\boldsymbol{J}^{n+1}\Delta t}(\boldsymbol{Q}^{m} - \boldsymbol{Q}^{n}) \tag{17}$$

where $\Delta^m\boldsymbol{Q} = \boldsymbol{Q}^{m+1} - \boldsymbol{Q}^{m}$. All time-implicit terms are kept on the left-hand side of Eq. (17), and the right-hand side of Eq. (17) contains all time-explicit terms, that is, terms that can be computed with available flow and structural information. During the subiteration in m, the structural solution and, thus, the grid remain untouched. This means that the Jacobians remain independent of m, or $\boldsymbol{J}^m = \boldsymbol{J}^{m+1} = \boldsymbol{J}^{n+1}$, so that Eq. (17) can be simplified to

$$\left[\frac{1}{\boldsymbol{J}^{n+1}}\left(\frac{1}{\Delta\tau} + \frac{1+\Psi}{\Delta t}\right)I + \frac{\partial R}{\partial \boldsymbol{Q}}\right]\Delta^m\boldsymbol{Q} = R(\boldsymbol{Q}) + \frac{1}{\boldsymbol{J}^{n+1}\Delta t}[\Psi\Delta^{n-1}\boldsymbol{Q} - (1+\Psi)(\boldsymbol{Q}^{m} - \boldsymbol{Q}^{n})] - \frac{(1+\Psi)\boldsymbol{Q}^n}{\Delta t}\left(\frac{1}{\boldsymbol{J}^{n+1}} - \frac{1}{\boldsymbol{J}^{n}}\right) \tag{18}$$

Note that Eq. (18) also assumes $\boldsymbol{J}^n = \boldsymbol{J}^{n-1}$. This reduces the formal temporal accuracy of Eq. (18) to first-order accuracy for dynamic meshes. This comes about because, at the time this aeroelastic version of CFL3D was developed, the decision was made to reduce in-core memory by not carrying an extra array for $\boldsymbol{J}^{n-1}$. Presently, in-core memory has become cheap and plentiful. More recent aeroelastic versions of CFL3D rectified this undesirable shortchanging of numerical accuracy for memory efficiency.

Grid Perturbation

Whereas the CAP-TSD method accounted for the aeroelastically deforming body surfaces with transpiration boundary conditions, the current coupling with an Euler/Navier–Stokes solver requires a grid perturbation method. This comes about because such structured-grid CFD methods solve the governing equations on volume grids that envelop a subject configuration. As that subject configuration deforms under loads, these body-conforming volume grids have to adapt dynamically as well. As mentioned before, the present aeroelastic version of CFL3D was developed for realistic High Speed Civil Transport configurations, which required dealing with multizone grids over wing/body/nacelle configurations at a minimum; there were several applications that involved canards and empennages as well. This requirement was compounded with demands on robustness, on low in-core memory, and on high computational efficiency. Some of the salient features of the grid perturbation method developed in response to these requirements are listed here. A master/slave concept couples field points (slaves) to the nearest solid surface node (master). This concept makes the multizone grid structure transparent to the user, that is, it obviates the need to establish explicitly grid connectivities across grid–zone interfaces, whether blocked or overlapped, by complex input decks. Memory requirements are kept low by trading a spring-analogy concept found in some previous aeroelastic versions of CFL3D with decay function concepts. Computational speed was achieved using fast transfinite interpolation. Details of this grid perturbation scheme can be found in Ref. 16.

Results

Computational Grid

A C–O-type grid was generated over a B-1-like configuration. This grid has 281 nodes in fuselage (or C direction), 137 nodes in span direction (or O direction), and 65 grid points in the direction away from the vehicle. The y^+ values for the first nodes off of the wall were two or smaller. These dimensions were based on extensive parametric studies on grid density and grid stretching in the HSR program.[17]

The geometric definition was based on CAD definitions of the B-1 B aircraft with nacelles omitted. Wind-tunnel data for flow-through nacelles correlated well with flight-test data for powered nacelles.[6] For static aeroelastic cases, computed flowfield results for a B-1-like wind-tunnel model without nacelles matched wind-tunnel data with flow-through nacelles quite well.[7] Based on these experiences, modeling the nacelles was deemed as adding geometric complexity, leading to increased grid size and to commensurately higher computational expenditure without significantly adding fidelity to the simulations of the fluid/structures interaction. Similar reasoning led to the elimination of the empennage from the computational model.

Static Aeroelasticty

The geometric (except for the aforementioned simplifications) as well as the structural definition, that is, the finite element model, were taken from the B-1B aircraft. The flow conditions were specified to match wind-tunnel data. The two sources of specifications and data are reconciled at their interface, namely, the computation of the generalized forces, which scale with the dynamic pressure (or point in the sky). There might be some differences in the flight and wind-tunnel flows due to Reynolds number effects; efforts to quantify these effects in the wind-tunnel tests were planned but not performed.[6]

Figure 1 compares computed flowfield results for a rigid and a static aeroelastic case. Depicted are contours of total pressure in crossplanes at 17 fuselage stations. The flow conditions ($M_\infty = 0.975$, $\alpha = 7.38$ deg, and $Re_c = 5.9 \times 10^6$) correspond to wind-tunnel conditions where LCO were observed. The static aeroelastic solution was computed for near-critical damping, which suppresses any dynamic aeroelastic motion. For the static aeroelastic solution, the wing tip bends up by about 32 in. full scale, which in scaled magnitude correlates well with wind-tunnel measurements for similar static aeoelastic cases. Note the resolution of the vortical flow in the wake of the juncture between fixed inner wing and the outer swing wing. A comparison of the contours indicates that the vortical flow is better developed for the rigid case than for the static aeroelastic case; for the latter, the wing is at a lower local effective angle of attack.

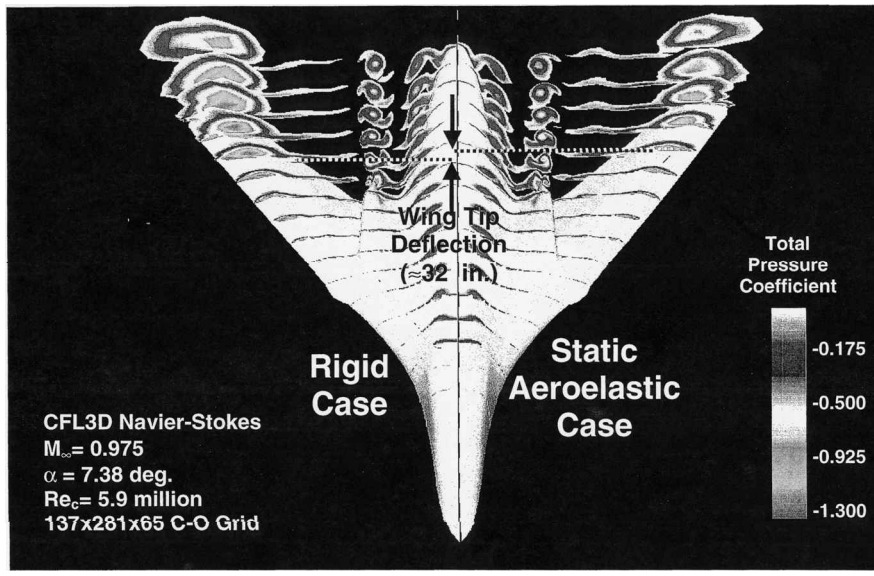

Fig. 1 Computed vortical flow over a B-1-like configuration with and without static aeroelastic structural response.

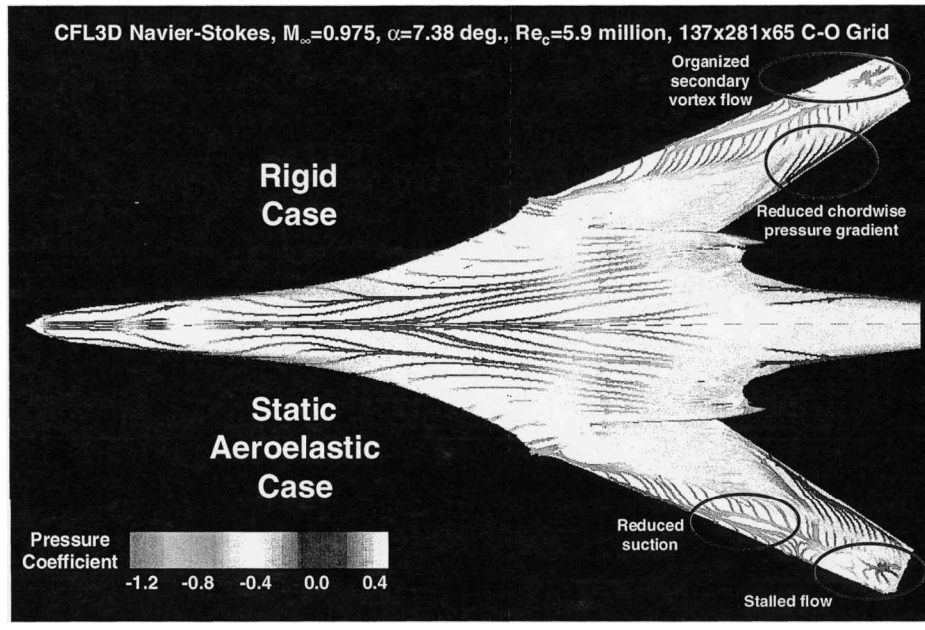

Fig. 2 Computed surface flow over a B-1-like configuration with and without static aeroelastic structural response.

For the same conditions as in Fig. 1, Fig. 2 compares the rigid with the static aeroelastic solution by means of surface streamlines, colored by static pressure. As observed before, compared to the static aeroelastic solution, the wing is at a higher angle of attack for the rigid case, leading to a better developed leading-edge vortex with a well-defined secondary vortex system. For the static aeroelastic case, the flow in the vicinity of the wing tip appears to be stalled.

The rigid solution in Figs. 1 and 2 is computed using local time stepping [Courant–Friedrichs–Lewy (CFL) number of 10], whereas the static aeroelastic solution was run to asymptotic steady state for 200 time steps using a global time step of about 0.005 s and five subiterations at each time level. The CFL number based on $\Delta\tau$ was 10, and the residual associated with the pseudo time term dropped by more than one order of magnitude. Doubling the number of subiterations had negligible effect on the convergence of the subiteration process. The convergence toward an asymptotic steady state of the time-accurate static aeroelastric solution is depicted in Fig. 3 by means of time histories for the four leading structural modes. The ranking is based on modal frequency and range from the lowest to the highest frequency. In all calculations presented here, only the first four structural modes were used. This cutoff was chosen because of a tradeoff between numerical efficiency and fidelity of the structural representation for the dynamic aeroelastic solutions. In previous studies of unsteady flow, a good resolution of a periodic motion was defined by about 40 time steps per cycle. The full-scale modal frequencies of the leading six structural modes are 2, 6, 12, 14, 20, and 24 Hz. This means that a time step size of 0.005 s satisfies the resolution requirement for the first two modes, that it is marginal for the third and fourth structural modes, and that it is clearly outside the parameter space for the fifth and sixth structural modes. The effect of the time step size on the quality of the computed dynamic fluid/structures interaction will be discussed subsequently. Check runs with all six structural modes indicated that the truncation of the modal representation has the effect of a shift toward lower angle of attack. As will be seen later on, in trying to capture the LCO phenomenon, this required running the dynamic aeroelastic

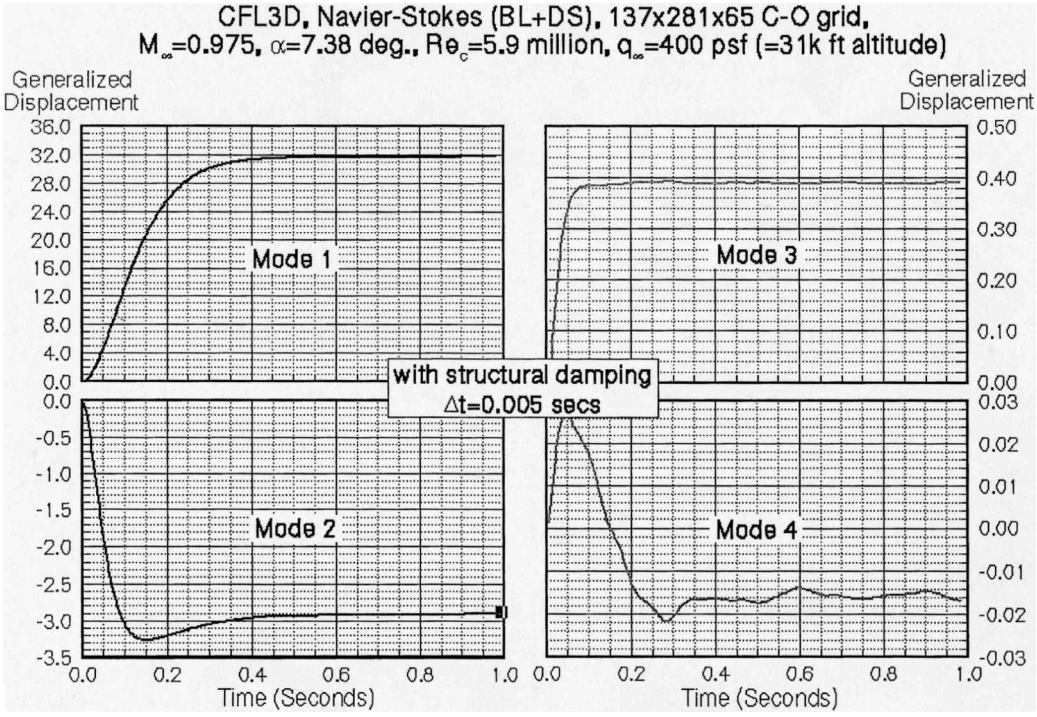

Fig. 3 Time histories of generalized displacements for static aeroelastic solution.

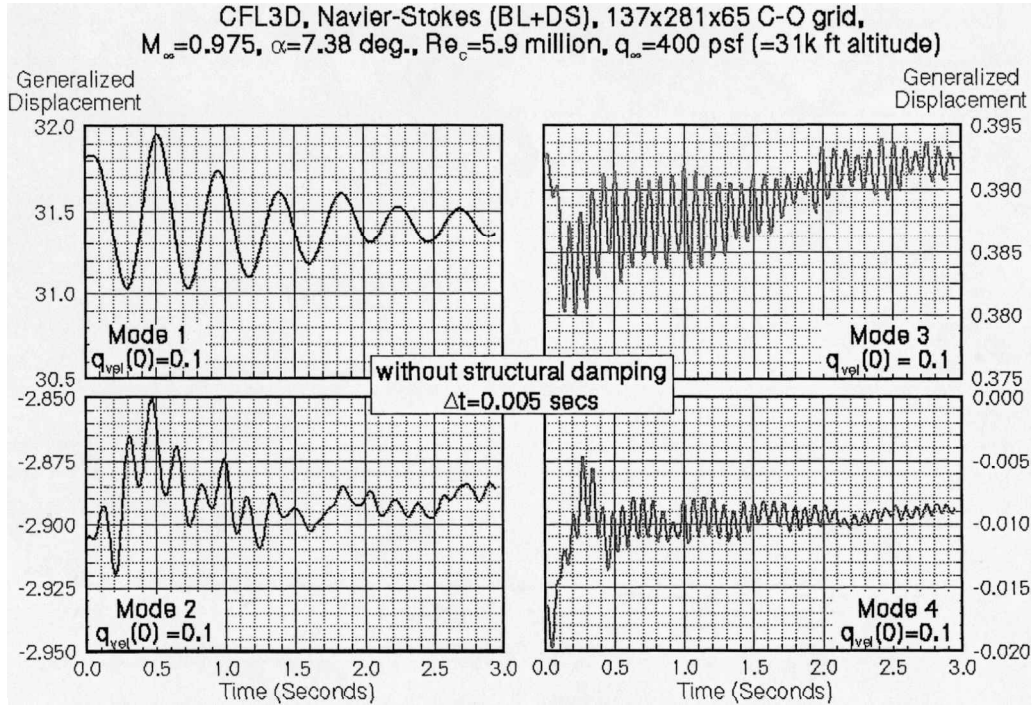

Fig. 4 Time histories of generalized displacements for dynamic aeroelastic solution triggered by initial generalized velocities.

solutions at an angle of attack higher than in the wind-tunnel experiment.

Dynamic Aeroelasticity

For a dynamic aeroelastic solution at nominal wind-tunnel LCO condition, Fig. 4 shows the time history for the four leading structural modes utilized in this study. This dynamic aeroelastic analysis was started from the asymptotic static aeroelastic solution discussed in Fig. 3 by specifying a small initial generalized velocity (0.1). Using finite generalized velocities reduces the transient phase compared to specifying initial values for generalized displacements.[9,15] Increasing the magnitude of the initial generalized velocity for only the first bending mode by an order of magnitude affects the transient phase, but leads to the same damped behavior seen in Fig. 4. To quantify the magnitude of the physical deflections, realize that the generalized displacement of the first bending mode, that is, mode 1, translates to the tip deflection measured in inches, that is, the wing tip oscillates with a maximum amplitude of about ± 1 in.

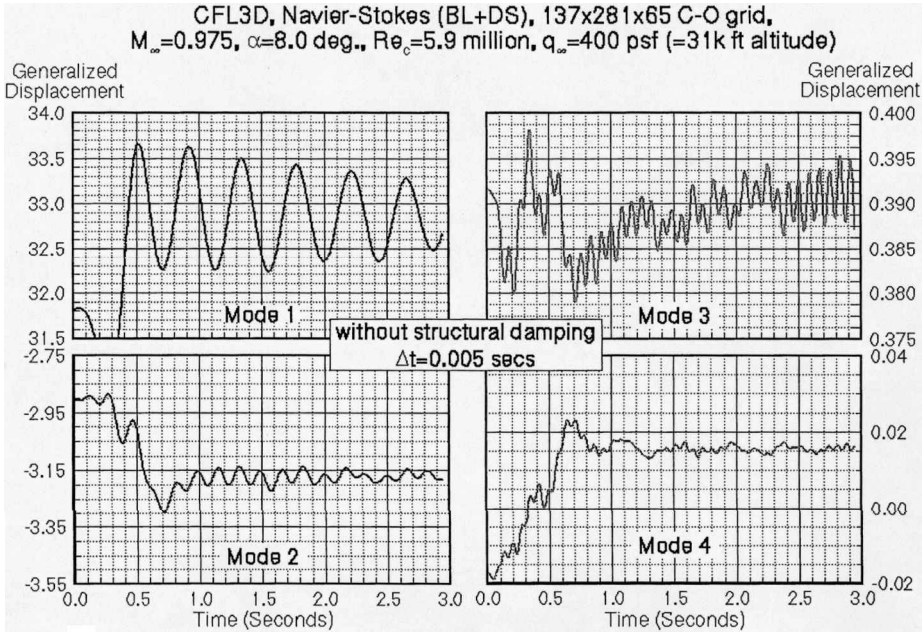

Fig. 5 Time histories of generalized displacements for dynamic aeroelastic solution initialized by change in angle of attack.

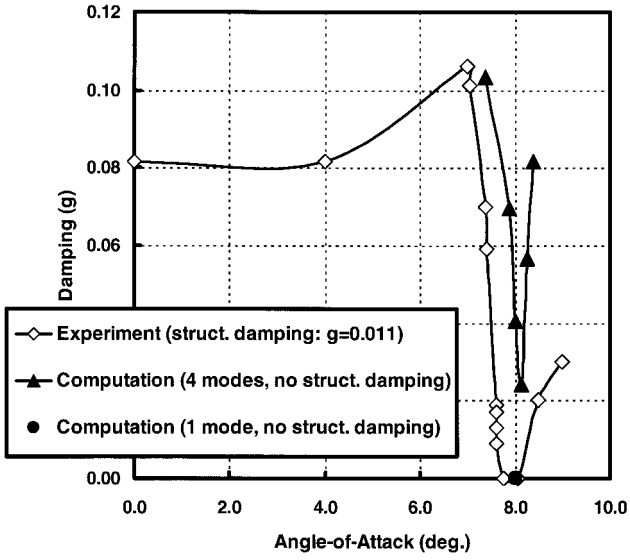

Fig. 6 Measured and computed aerodynamic damping.

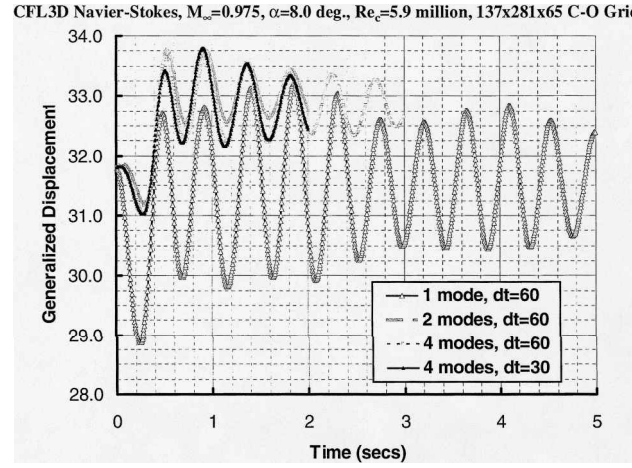

Fig. 7 Effect of computational time step size on structural mode evolution.

From the experiment,[6] it is known that the LCO phenomenon is very sensitive to the angle of attack; it was observed only within an angle-of-attack range of less than half of a degree. This led to a systematic variation of the angle of attack in the current nonlinear aeroelastic analyses. All of these cases were started without specifying any initial values for generalized displacements or generalized velocities; just letting the solution proceed from the static aeroelastic solution for $\alpha = 7.38$ deg resulted in a dynamic response. With the same layout as Fig. 4, Fig. 5 shows the time histories for $\alpha = 8$ deg. The response of the first bending mode still indicates damping, yet it appears to be significantly less than for $\alpha = 7.38$ deg in Fig. 4. Also note the beating in the third bending, which is characteristic for LCO.

Figure 6 summarizes computed and measured[6] aerodynamic damping for $0 \leq \alpha < 9$ deg. Whereas all computations are carried out without any structural damping, the structural damping for the wind-tunnel model is estimated to be about 1.1%. The computations with the leading four structural modes capture the trend observed in the experiment: for $7 \leq \alpha < 8.5$ deg, there is a narrow dip in aerodynamic damping that is indicative of LCO, whereas for $7.3 < \alpha < 7.9$ deg, LCO (i.e., sustained structural response with beating but no buildup in amplitude) that correspond to zero aerodynamic damping were observed in the wind-tunnel tests. The numerical solutions fall short of actually indicating LCO; there is always residual aerodynamic damping. Also shown in Fig. 6 is a solution in which only the leading bending mode was used. For this mode, the time history of the generalized displacement over more than 10 cycles indicated LCO because no aerodynamic damping could be established based on the beating, that is, growing and decaying, amplitudes.

Figure 7 displays the time histories of the first bending mode as recorded for four different solutions. These solutions are 1) a solution involving the four leading structural modes with the default time step size of 0.005 s; 2) a solution involving the four leading structural modes computed with half the default computational time step size, that is, $\Delta t = 0.0025$ s; 3) a solution involving only the first two structural modes computed with the default time step size of 0.005 s; and 4) the LCO solution computed with the default time step size of 0.005 s and retaining only the first bending mode. The single structural mode solution resolves each cycle of structural response

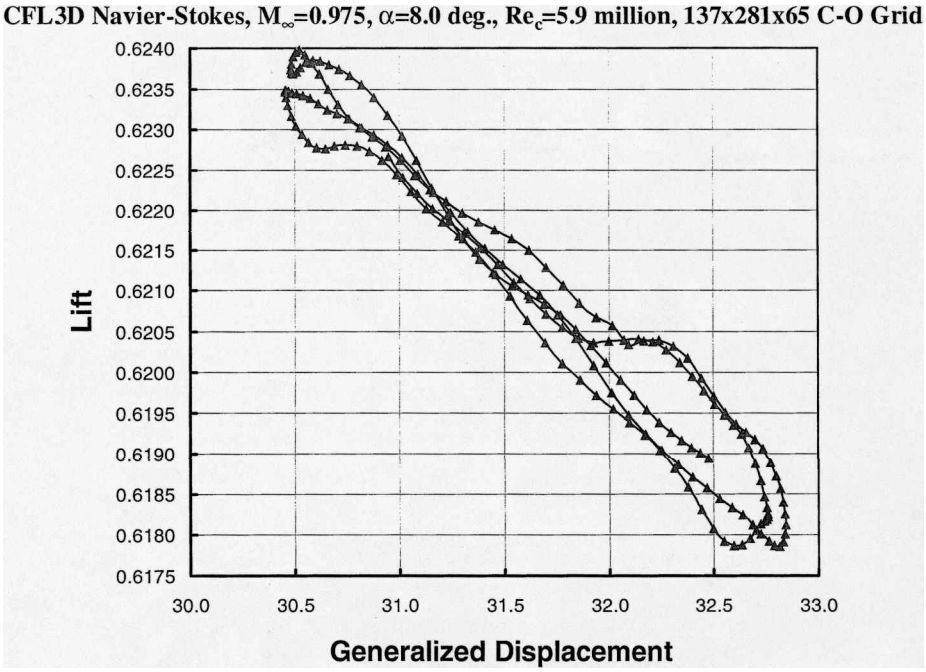

Fig. 8 Phase diagram, lift vs generalized displacement of first mode.

with an average of about 100 time steps. Given that this single-mode solution is the only aeroelastic analysis that suggests LCO-like behavior, one could conclude that this represents about the right temporal resolution of the fluid/structures interaction for capturing the B-1 LCO behavior. Whereas the first bending mode gets as well resolved, if not better (for the solution with $\Delta t = 0.0025$ s), in the other three solutions, the higher-frequency modes experience a lower resolution. It is conjectured that the error introduced by not properly resolving the higher-frequency modes aliases into the first bending mode, suppressing the development of an LCO-like structural response observed for the single-mode solution.

Because a damping estimate for the time history of the first bending mode only solution in Fig. 7 is inconclusive, a phase diagram analysis is used in Fig. 8 to determine whether this single-mode solution indeed indicates LCO. In Fig. 8, lift is plotted as a function of the generalized displacement of the first bending mode. As the wing moves up, the local angle of attack gets reduced, weakening the leading-edge vortex and leading to a reduction in lift. As the wing moves downward, the local angle of attack increases as does the vortex-induced lift. The lift traces are recorded for several cycles of structural motion and generally describe a figure-eight-like pattern. In the lower part of this pattern, the structural motion leads the lift response. This extracts energy from the structural system. In the upper portion of the traces, lift leads the structural response, thus injecting energy into the structural system. For LCO, the area circumscribed by these two components of the figure-eight pattern are of about equal size. It is obvious from the phase diagram that the overall system is still damped as the energy drawn from structural system during the down-bending wing motion outweighs the mechanical work the flow exerts on the wing structure during the up-bending phase. As a corollary, note the high degree of nonlinearity in this fluid/structure interaction as indicated by the small loop at near-maximum lift.

Figure 9 summarizes for flight and wind-tunnel tests the LCO behavior and for CFD the LCO-like behavior for the B-1B and for its wind-tunnel and CFD approximations. There is good agreement regarding the oscillation frequency among all three data sets. Note that the wind-tunnel model LCO maximum amplitude is half of that measured in flight, whereas the computed LCO solution predicts wing tip amplitudes that are an order of magnitude smaller than those recorded during flight. Some of the discrepancies in the measured and computed amplitudes might be due to different load conditions.

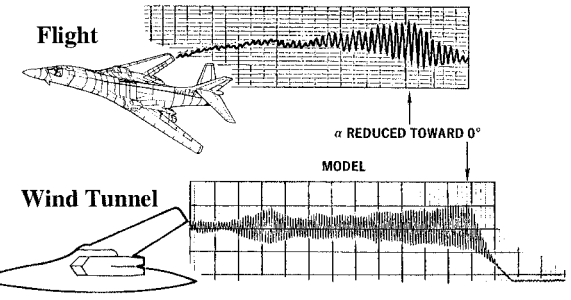

	Sweep Angle (deg.)	AOA - Fuselage	Mach Number	Altitude (ft, full scale)	Reynolds Number (million)	Oscillation Frequency (Hz, full scale)	Tip Amplitude (in., full scale)
CFD	67.5	8	0.975	31K	5.9	2.2	+/- 1.5
Wind Tunnel	67.5	7.38	0.975	35K	5.9	2	+/-7.6
Aircraft	66.9	8.1 - 8.4	0.9 - 0.95	31K - 33.3K	50	2.1	+/-15

Fig. 9 Frequencies and amplitudes of LCO phenomenon as observed in flight, in wind-tunnel tests, and in computations.

For instance, in flight, the LCO phenomenon is encountered during transonic turn, which adds centrifugal forces to the aircraft loads that occur in neither the wind-tunnel test nor in the nonlinear analysis.

Figure 10 shows an experimental oil flow pattern along with measured steady pressure distributions at selected span stations.[6] These data were taken at an angle of attack low enough to avoid LCO. The quality of the photograph allows one only to discern some rough overall flow patterns, which become easier to interpret when taken in conjunction with the computed surface flow patterns in Fig. 11. Figure 11 shows four snapshots taken during the LCO-like motion as computed in the first bending mode only solution discussed earlier. These snapshots are taken at the wing maximum bent-up position (peak), at the maximum bent-down position (trough), and at the maximum wing speed conditions on its way up or down. The instantaneous streamlines are colored with static pressure. The computed separation and reattachment lines attributed to secondary vortex flow velocity compare qualitatively well with the experimental surface flow pattern in Fig. 10. In addition, the computed surface flow pattern shed some light on the interaction of vortical flow with the wing structural motion. At the wing-down (trough) position, the effective local angle of attack is at a maximum, leading to strong vortical flow as indicated by a well-formed secondary

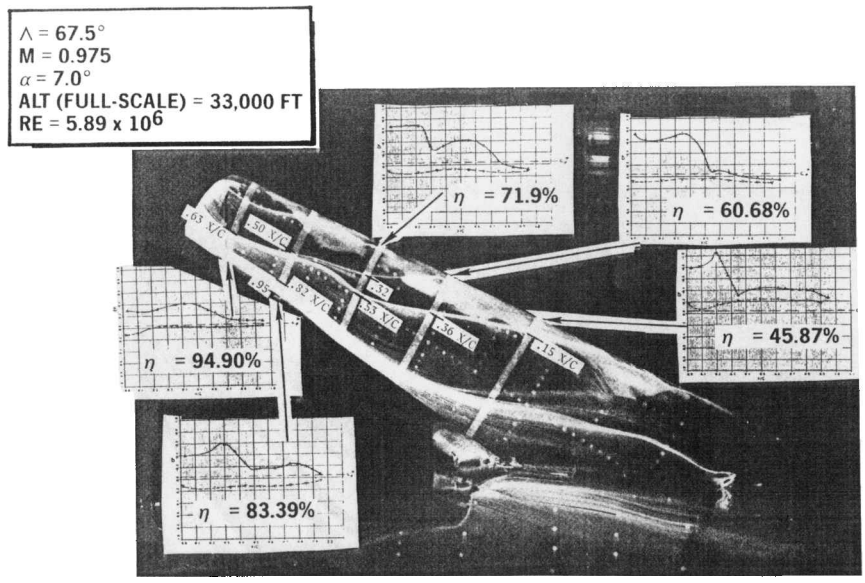

Fig. 10 Surface oilflow and surface pressures for B-1-like configuration in wind-tunnel test.

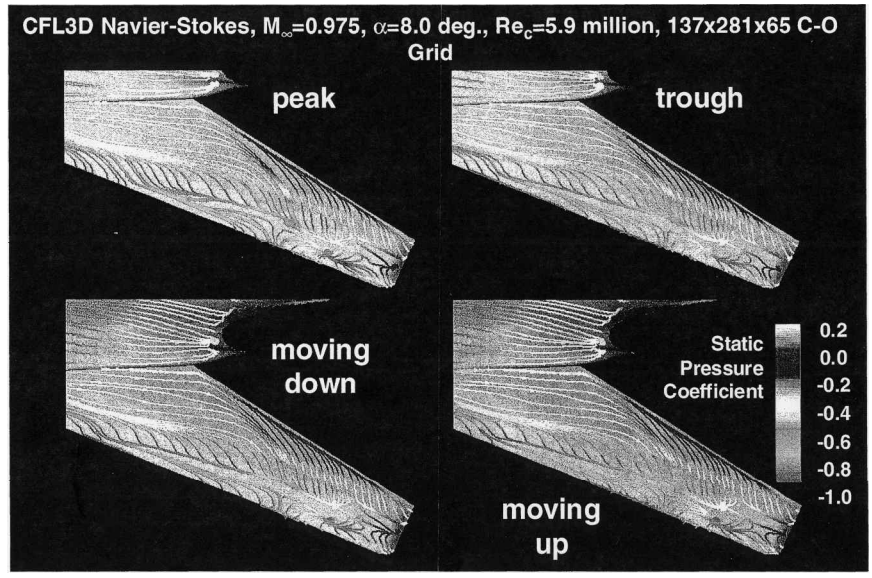

Fig. 11 Computed instantaneous streamlines for B-1 wing undergoing LCO-like motion.

vortex system (judged by its footprint in terms of separation and reattachment lines) and a maximum of nonlinear vortex lift. At the wing-up position (peak), the local angle of attack is at a minimum, leading to a weaker vortical system and less vortex-induced lift.

Conclusions

One of the more recent aeroelastic versions of the Euler/Navier–Stokes solver CFL3D was applied to LCO simulations for a B-1-like configuration. Although falling short in predicting a true LCO phenomenon, the predicted aerodynamic damping closely matched experimentally determined trends. Proper temporal resolution of the fluids/structures interaction was identified as key to capturing the LCO phenomenon. Several areas improvement to future aeroleastic versions of CFL3D were suggested.

Acknowledgments

This work was funded by Boeing under Independent Research and Development. Its results were contributed to the evaluation of nonlinear aeroelasticity analysis methods sponsored by the Aerodynamics–Structures–Control Interaction consortium under the leadership of Lawrence Huttsell (Air Force Research Laboratory, Wright–Patterson Air Force Base, Ohio). The computing resources were provided by the Numerical Aerospace Simulation facility of NASA under a technology transfer arrangement. The many fruitful discussions with Myles L. Baker and Joseph P. Giesing, both of The Boeing Company, Phantom Works, Long Beach, California, are gratefully acknowledged.

References

[1] Rodden, W. P., and Johnson, E. H., "MSC/NASTRAN Aeroelastic Analysis User's Guide," Ver. 68, MacNeal–Schwendler Corp., 1994.

[2] Albano, E., and Rodden, W. P., "A Doublet-Lattice Method for Calculating Lift Distributions on Oscillating Surfaces in Subsonic Flows," *AIAA Journal*, Vol. 7, No. 7, 1969, pp. 279–285.

[3] Biedron, R. T., and Thomas, J. L., "A Generalized Patched-Grid Algorithm with Application to the F-18 Forebody with Actuated Control Strake," *Computing Systems in Engineering*, Vol. 1, Nos. 2–4, 1990, pp. 563–576.

[4] Thomas, J. L., Krist, S. L., and Anderson, W. K.,"Navier–Stokes Computation of Vortical Flows over Low Aspect Ratio Wings," *AIAA Journal*, Vol. 28, No. 4, 1990, pp. 205–212.

[5] Vatsa, V. N., Thomas, J. L., and Wedan, B. W., "Navier–Stokes Computations of a Prolate Spheroid at Angle of Attack," *Journal of Aircraft*, Vol. 26, No. 11, 1989, pp. 986–993.

[6]Dobbs, S. K., Miller, G. D., and Stevenson, J. R., "Self-Induced Oscillation Wind-Tunnel Test of a Variable Sweep Wing," AIAA Paper 85-0739-CP, April 1985.

[7]Guruswamy, G. P., "Vortical Flow Computations on a Flexible Blended Wing-Body Configuration," *AIAA Journal*, Vol. 30, No. 10, 1992, pp. 2497–2503.

[8]Robinson, B. A., Batina, J. T., and Yang, H. T. Y., "Aeroelastic Analysis of Wings Using the Euler Equations with a Deforming Mesh," *Journal of Aircraft*, Vol. 28, No. 11, 1991, pp. 781–788.

[9]Lee-Rausch, E. M., and Batina, J. T., "Wing Flutter Boundary Prediction Using Unsteady Euler Aerodynamic Method," *Journal of Aircraft*, Vol. 32, No. 2, 1995, pp. 416–422.

[10]Lee-Rausch, E. M., and Batina, J. T., "Wing Flutter Computations Using an Aerodynamic Model Based on the Navier–Stokes Equations," *Journal of Aircraft*, Vol. 33, No. 6, 1996, pp. 1139–1147.

[11]Bartels, R., "An Elasticity-Based Mesh Scheme Applied to the Computation of Unsteady Three-Dimensional Spoiler and Aeroelastic Problems," AIAA Paper 99-3301, June 1999.

[12]Baker, M. L., Mendoza, R., and Hartwich, P. M., "Transonic Aeroelastic Analysis of a High-Speed Transport Wind-Tunnel Model," AIAA Paper 99-1217, April 1999.

[13]Kuruvila, G., Hartwich, P. M., and Baker, M. L., "The Effect of Aeroelasticity on the Aerodynamic Performance of the TCA," *1998 NASA High-Speed Research Program—Aerodynamic Performance Workshop*, NASA CDCP-1006, Vol. 1, Pt. 2, 1998, pp. 1589–1648.

[14]Rumsey, C. L., Sanetrik, M. D., Biedron, R. T., Melson, N. D., and Parlette, E. B., "Efficiency and Accuracy of Time-Accurate Turbulent Navier–Stokes Computations," AIAA Paper 95-1835-CP, June 1995.

[15]Cunningham, H. J., Batina, J. T., and Bennett, R. M., "Modern Wing Flutter Analysis by Computational Fluid Dynamics Methods," *Journal of Aircraft*, Vol. 25, No. 10, 1988, pp. 962–968.

[16]Hartwich, P. M., and Agrawal, S., "Method for Perturbing Multiblock Patched Grids in Aeroelastic and Design Optimization Applications," AIAA Paper 97-2038-CP, June 1997.

[17]Mendoza, R., Shieh, C. F., and Sundaram, P., "Flowfield Studies for the TCA/NCV Configurations," *1999 NASA High-Speed Research Program—Aerodynamic Performance Workshop* NASA CP-1999-209704, Vol. 1, Pt. 2, 1999, pp. 1289–1364.